Research Square

Preprints are preliminary reports that have not undergone peer review.
They should not be considered conclusive, used to inform clinical practice,
or referenced by the media as validated information.

Two-sample Mendelian randomization combined with GraphBAN reveals druggable prognostic genes and risk stratification in kidney renal clear cell carcinoma

Huaru Zhang
Guangzhou Red Cross Hospital, Guangzhou Red Cross Hospital of Jinan University
Tao Zhang
Guangzhou Red Cross Hospital, Guangzhou Red Cross Hospital of Jinan University
Youlong Lu
Guangzhou Red Cross Hospital, Guangzhou Red Cross Hospital of Jinan University
Cheng Li
Guangzhou Red Cross Hospital, Guangzhou Red Cross Hospital of Jinan University
Yujian Li
Guangzhou Red Cross Hospital, Guangzhou Red Cross Hospital of Jinan University
Xinjun Deng
dengxinjun30@163.com

Guangzhou Red Cross Hospital, Guangzhou Red Cross Hospital of Jinan University

Research Article

Keywords: Carcinoma, Renal Cell, Genome-Wide Association Study, Immunotherapy, Molecular Dynamics Simulation, Tumor Microenvironment

Posted Date: May 29th, 2026

DOI: https://doi.org/10.21203/rs.3.rs-9651090/v1

License: This work is licensed under a Creative Commons Attribution 4.0 International License.
Read Full License

Additional Declarations: No competing interests reported.

Abstract

Purpose: Kidney renal clear cell carcinoma (KIRC) remains associated with poor outcomes in advanced disease, and robust prognostic biomarkers and actionable therapeutic targets are still lacking. This study aimed to identify druggable genes causally associated with KIRC and to establish a clinically relevant risk stratification model. Methods: We integrated TCGA-KIRC transcriptomic data, FinnGen GWAS summary statistics, curated druggable gene sets, differential expression analysis, two-sample Mendelian randomization, Cox and LASSO modeling, immune and mutation profiling, and GraphBAN-based compound prediction with molecular docking and molecular dynamics validation.

Results: We identified 129 druggable genes with significant causal associations with KIRC and established a four-gene prognostic signature comprising ALDH6A1, AMH, ASIC3, and PLK1. The resulting risk model effectively stratified patients into high- and low-risk groups, with poorer survival in the high-risk group and good predictive performance in both internal and external cohorts (AUC > 0.70). High-risk tumors also showed distinct pathway enrichment, an altered immune microenvironment, lower predicted immunotherapy response, and a higher somatic mutation burden. In addition, several candidate compounds showed favorable binding to prognostic targets.

Conclusions: These findings identify clinically relevant druggable prognostic genes in KIRC and provide a useful framework for risk assessment, target discovery, and individualized therapeutic exploration.

1. Introduction

Renal cell carcinoma (RCC), a heterogeneous type of renal cortical malignancy derived from renal tubular epithelial lesions, exhibits diverse clinical, morphological, and genetic traits(Rysz et al. 2021). Globally, an estimated 431,288 new kidney cancer cases were documented in 2022, among which RCC constituted 90% of the total diagnoses. As the most common subtype of RCC that accounts for more than 70% of all cases, KIRC presents a grave hazard to global public health due to its unique pathological characteristics and unfavorable clinical prognosis(Xiong et al. 2022; Patergnani et al. 2020; Cancer Genome Atlas Research 2013; Bukavina et al. 2022). Characterized by VHL gene inactivation at the 3p25 locus of chromosome 3, metabolic reprogramming involving aerobic glycolysis and abnormal amino acid metabolism, and interactions with an unfavorable tumor microenvironment (TME), KIRC often presents with hemorrhage, cystic degeneration, and necrosis in advanced stages—severe pathological manifestations that drastically reduces patients' quality of life(Nezami et al. 2025; Lucarelli et al. 2019). Despite the evolution of therapeutic strategies from cytokine-based immunomodulation to VEGF-targeted therapy and immune checkpoint inhibitors, KIRC remains largely refractory to radiotherapy, chemotherapy, and many immunotherapies, with surgical resection still being the mainstay of treatment(Berquist et al. 2019; Zhang et al. 2021). Alarmingly, nearly one-third of patients are diagnosed with metastatic disease, and the 5-year survival rate after metastasis is only 10%, highlighting the urgent need for effective prognostic biomarkers and novel druggable targets(Bex et al. 2018; van den Heuvel et al. 2019).

The "druggable genome" concept, encompassing genes encoding drug-modifiable proteins, has emerged as a cornerstone for targeted therapy development(Finan et al. 2017) . Considering the poor prognosis of metastatic KIRC, despite advances in targeted therapy, the emergence of drug resistance and severe adverse events underscores the need for novel druggable targets beyond those in clinical development(Rustum et al. 2023; van den Heuvel et al. 2019; Damayanti et al. 2024; Lasorsa et al. 2023), yet relevant research remains scarce. In-depth exploration of druggable genes is critical to advancing KIRC's clinical therapeutic paradigm. Current targeted agents, notably VEGF/VEGFR pathway inhibitors, are standard for KIRC but drug resistance remains pervasive(Posadas et al. 2013). While immune checkpoint inhibitors (ICIs) have transformed advanced KIRC management, they exhibit marked inter-patient heterogeneity, benefiting only a subset(Lasorsa et al. 2023) . Hence, systematic identification of novel actionable molecular targets is key to overcoming current therapeutic limitations and developing innovative combination/salvage regimens.

As a powerful analytical method relying on genetic variants as instrumental variables (IVs) for confounding reduction, Mendelian randomization (MR) has achieved successful application in the identification of tumor risk factors and potential therapeutic candidates, based on strict adherence to the core tenets of relevance, independence, and exclusion restriction(Emdin et al. 2017) . MR has been applied to identify KIRC risk factors, pathogenic genes, and therapeutic targets(Chen et al. 2024; Zheng et al. 2024; Lin et al. 2024) . A sex-specific MR analysis identified a causal link between specific circulating inflammatory cytokines (e.g., MIP-1β) and male RCC risk, implicating systemic inflammation as a potential pathogenic factor for KIRC(Tao et al. 2023). Moreover, integrated MR-KIRC cohort data verified that key MAPK pathway genetic variants causally link to KIRC susceptibility, patient prognosis and tumor immune microenvironment traits(Zheng et al. 2024).

In this study, we integrated KIRC transcriptomic data, genome-wide association study (GWAS) datasets, and curated druggable gene sets to address existing gaps. Through a comprehensive pipeline combining differential expression analysis and MR, we systematically screened and validated druggable genes with significant prognostic value in KIRC, and subsequently constructing a robust risk stratification model. Further investigations revealed close correlations between the druggable gene-related risk score and key molecular features, including TME composition, immunotherapeutic response efficacy, and somatic mutation profiles. To accelerate translational research, we employed the GraphBAN model to predict the interaction probabilities between potential therapeutic compounds and the identified prognostic genes. Collectively, our findings shed new light on the molecular underpinnings of KIRC progression while also furnishing a reliable risk stratification tool for clinical practice. Moreover, molecular docking and dynamics simulations evaluated drug-prognostic gene binding affinity, laying a solid theoretical foundation for developing innovative targeted therapies to improve KIRC diagnosis, treatment and prognosis.

2. Materials and Methods

2.1 Data sources

Transcriptomic data and clinical information of KIRC (TCGA-KIRC dataset) were retrieved from The Cancer Genome Atlas (TCGA) database (https://www.cancer.gov/ccg/research/genome-sequencing/tcga), which included data from 534 tumor tissue samples of KIRC patients with survival information and 71 normal tissue samples from healthy individuals. Subsequently, the E-MTAB-1980 dataset was retrieved from the ArrayExpress database (https://www.ebi.ac.uk/biostudies/arrayexpress) as an external validation set, containing data from 78 tumor tissue samples of alive KIRC patients and 23 tumor tissue samples of dead KIRC patients. Annotation files were acquired from the UCSC Xena platform (https://xena.ucsc.edu/). Additionally, summary data on the genetic correlation of renal cell carcinoma and its subtypes (Release 12, R12 dataset) were acquired from the FinnGen League, with the download link: https://storage.googleapis.com/finngen-public-data-r12/summary_stats/release/finngen_R12_C3_KIDNEY_CLEAR_CELL_CARCINOMA_EXALLC.gz. The R12 dataset comprises 1,499 Finnish case samples, 378,749 control samples, and 20,461,800 non-synonymous single nucleotide polymorphisms (nSNPs). Finally, a total of 4,463 druggable genes were obtained from the reference(Finan et al. 2017) , and 3,953 druggable genes were retrieved from the Drug-Gene Interaction Database (DGIdb, https://www.dgidb.org/) (v4.2.0). After merging and removing duplicates, 5,883 druggable genes were obtained (**Supplementary Table 1**). Data acquisition was performed on July 23, 2025.

2.2 Differential expression analysis

The DESeq2 package (v1.40.2)(Love et al. 2014) was used to identify the differentially expressed genes (DEGs) between control samples and KIRC samples in the TCGA-KIRC dataset ($|\log_2$ fold change (FC)$| > 2$, adjusted $p < 0.05$). To further obtain DEGs with druggable signatures, the ggVenn package (v0.1.10) was used to identify the intersection of DEGs and the 5,883 druggable genes, which were defined as candidate genes.

2.3 Screening IVs and MR analysis

To identify candidate genes with a marked causal relationship with KIRC, where KIRC and the candidate genes were treated as the outcome and exposure factors, respectively. First, to ensure the reliability of IVs (SNPs), the study employed the extract_instruments function from the TwoSampleMR package (v0.6.15)(Zheng et al. 2022) to retrieve data on candidate genes and KIRC, followed by IV screening. The specific steps were as follows: IVs significantly associated with candidate genes were selected using a threshold of $p < 5 \times 10^{-6}$. The linkage disequilibrium (LD) exclusion function (clump = TRUE) was enabled, with parameters set to $R^2 < 0.001$ and distances > 10 kb, to eliminate IVs with LD. Combined with KIRC GWAS data, IVs significantly associated with KIRC were further excluded. The strength of each IV was evaluated by calculating the F-statistic; weak IVs with an F-statistic < 10 were removed, and exposure factors with fewer than three IVs (nSNP < 3) were also excluded.

$$F\text{-}value=(\frac{\beta^2}{SE^2})$$

Among these, β represented the effect size of the allele, and SE denoted the standard error. Next, the harmonise_data function was used to harmonize effect sizes and effect alleles. Afterwards, the mr function integrated five algorithms for MR analysis. In detail, MR Egger(Bowden et al. 2015) , weighted median(Bowden et al. 2016) , inverse variance weighted (IVW)(Burgess et al. 2015), simple mode(Hemani et al. 2018) , and weighted mode(Hartwig et al. 2017) were applied to analyze the marked causal relationship between candidate genes and KIRC. Notably, IVW served as the primary algorithm for result evaluation. The weight formula for IVW was as follows:

$$wi=\frac{1}{SE_i^2}$$

Here, wi was the weight of the i-th IV, and SE_i^2 was the standard error of the estimated value of the i-th IV. To ensure the robustness of the findings, further evaluations were performed. The mr_heterogeneity function was employed to examine whether there were marked differences in the effects of different IVs on KIRC ($p > 0.05$). If heterogeneity was present, random-effects IVW was used for MR analysis; otherwise, fixed-effects IVW was applied. The mr_presso function of the MRPRESSO package (v1.0) (Yang et al. 2023) and the mr_pleiotropy_test of the TwoSampleMR package (v0.6.15) were used to assess the presence of confounding factors ($p > 0.05$); if confounding factors existed, the corresponding candidate genes were excluded. The direction of the causal relationship between candidate genes and KIRC was determined using the Steiger directionality test (directionality_test function), and only candidate genes with a "TRUE" result were retained ($p < 0.05$). Furthermore, the mr_scatter_plots function was used to generate scatter plots for assessing the correlations between candidate genes and KIRC, and the mr_forest_plot function was employed to produce forest plots for estimating the association between candidate genes and KIRC risk. The mr_funnel_plot function was utilized to create funnel plots, which visualized the IVW estimates of SNPs against 1/standard error ($1/SE_{IV}$). The mr_leaveoneout function was employed to execute the leave-one-out (LOO) analysis to verify whether a single SNP could alter the combined effect of all SNPs.

2.4 Functional enrichment and interaction network of candidate genes

To further investigate the pathways enriched in the candidate genes, the clusterProfiler package (v4.8.3) (Yu et al. 2012) was employed to perform Gene Ontology (GO) and Kyoto Encyclopedia of Genes and Genomes (KEGG) enrichment analyses (adjusted $p < 0.05$). To understand the interaction between proteins encoded by candidate genes, these genes were imported into the STRING (https://string-db.org/) with a confidence score threshold set to 0.4.

2.5 Recognition of prognostic genes

To identify genes markedly associated with the survival of KIRC, in the TCGA-KIRC dataset, univariate Cox regression analysis was performed on the candidate genes using the coxph function of the survival package (v3.7.0)(Lei et al. 2023) (hazard ratio (HR) ≠ 1, $p < 0.01$). To reduce the interference caused by extreme values, 13 samples with a survival time of fewer than 30 days were excluded from the cohort, with the remaining 521 KIRC samples being subjected to survival-associated analyses. The cox.zph function was then used to conduct the proportional hazards (PH) assumption test, aiming to verify whether each variable satisfied the proportional hazards assumption ($p > 0.05$). To ensure the consistency of the association between candidate genes and KIRC risk, only genes with consistent directionality between HRs (derived from univariate regression analysis) and ORs (derived from MR analysis) were retained. Subsequently, the glmnet package (v4.1.8)(Engebretsen et al. 2019) was employed to perform least absolute shrinkage and selection operator (LASSO) regression analysis (10-fold cross-validation). When the lambda value of the model was minimized, model genes with variable coefficients not penalized to zero were obtained as druggable signature-associated prognostic genes in KIRC.

2.6 Establishment of a risk model

The risk score for prognostic genes was computed to construct the risk model, with coef denoting the risk coefficient (coef) pertinent to each prognostic gene, and expression (expr) signifying the expression level of each corresponding prognostic gene.

$$risk\ score = \sum_{i=1}^{n} coef(gene_i) \times expr(gene_i)$$

Based on the optimal cut-off value, the KIRC samples from the TCGA-KIRC dataset were divided into high-risk and low-risk groups. The survminer package (v0.4.9)(Kuzuoglu-Ozturk et al. 2021) was employed to generate the Kaplan-Meier (KM) survival curves to compare the differences in survival status between the risk groups (log-rank test). Furthermore, the pROC package (v1.18.5)(Robin et al. 2011) was adopted to plot receiver operating characteristic (ROC) curves to evaluate the predictive performance of the model. The expression profiles of prognostic genes were analyzed across different risk groups. Finally, it should be noted that to further validate the results, the above analyses were replicated in the external validation set. Ultimately, to investigate the association between KIRC and risk scores, differences in risk scores among subgroups stratified by various clinicopathological features were compared.

2.7 Gene set enrichment analysis (GSEA)

To investigate which pathways are affected by the risk score, DEGs between risk groups were sorted in descending order based on log_2FC to generate a gene ranking list. The KEGG background gene set was retrieved from the MSigDB (https://www.gsea-msigdb.org/gsea/msigdb) (species = 'Homo sapiens',

category = 'C2', subcategory = "CP: KEGG"). Subsequently, GSEA was then performed via the clusterProfiler package (v4.8.3) (|normalized enrichment score (NES)| > 1, $p < 0.05$, false discovery rate (FDR) < 0.25).

2.8 Risk groups-based analysis of immune features

The Xcell algorithm in the IOBR package (v0.99)(Zeng et al. 2021) was employed to assess differences in infiltration scores of 34 types of immune cells between risk groups. Furthermore, the corrplot (v0.92) (Berquist et al. 2019) was used to explore Spearman rank correlations between differentially infiltrated immune cells, as well as between these cells and prognostic genes/risk scores (|correlation coefficient (cor)| > 0.3, $p < 0.05$). Furthermore, the response to immunotherapy was assessed between risk groups. Specifically, based on the ESTIMATE database (https://bioinformatics.mdanderson.org/estimate/), the ESTIMATE package (v1.0.13)(Yoshihara et al. 2013) was employed to compute the ESTIMATE, stromal, immune, and tumor purity scores to appraise the response to immunotherapy within the risk groups. Additionally, using the Tumor Immune Dysfunction and Exclusion (TIDE) platform (http://tide.dfci.harvard.edu/), the differences in the expression profiles of immune checkpoint (CD274), cells (cancer-associated fibroblasts (CAFs), M2-type tumor-associated macrophages (M2-TAMs), CD8+ T cells, myeloid-derived suppressor cells (MDSCs), dysfunction score, exclusion score, IFNG, Merck18, microsatellite instability, and TIDE signatures between risk groups were further analyzed. Furthermore, based on the TIDE prediction results, the proportions of immunotherapy responders and non-responders between risk groups were calculated, aiming to further evaluate the potential impact of different metastatic statuses on immune responses.

2.9 Mutation analysis

To compare differences in somatic mutations between the risk groups, somatic mutation analysis was performed using the Amutations package (v0.4.0)(Radenbaugh et al. 2014) , based on the somatic mutation data of KIRC samples obtained from the UCSC XENA platform (http://xena.ucsc.edu/). Moreover, the distribution of tumor mutation burden (TMB) between the risk groups was analyzed.

2.10 Potential drugs predicted by the GraphBAN model and their molecular docking

To investigate the clinical potential of prognostic genes, a graph-based inductive learning framework was constructed using GraphBAN analysis to predict compound-protein interactions (CPIs). Based on two datasets (BindingDB and BioSNAP), extended-connectivity fingerprints for compounds (ECFP4, depth 4) were extracted via RDKit, while 3-mer frequency features of proteins were processed using the kmer package (v1.1.3). Data were partitioned into source domains (60% clusters) and target domains (40% clusters, further split into 80% for training and 20% for testing) via scikit-learn single-linkage clustering (threshold $\gamma = 0.5$). The model adopted a teacher-student architecture: the teacher module leveraged a graph autoencoder (GAE) implemented in the PyTorch framework (https://pytorch.org/) to learn network structures; the student module fused compound features (from GCN and ChemBERTa) and protein features (from CNN and ESM) via a bilinear attention network (BAN), with cross-domain

differences addressed using a conditional domain-adversarial network (CDAN). Hyperparameters were optimized via random search during training (batch size = 32; teacher GAE learning rate = 1×10^{-3}; student learning rate = 1×10^{-4}; dropout rate = 0.2; total loss function = BCE, combining KD loss and CDAN loss). The GraphBAN model, trained on BindingDB, BioSNAP, and KIBA datasets, was used to predict 1,615 drugs from the ZINC-FDA dataset (https://zinc.docking.org/substances/subsets/fda/). Drugs were filtered using an interaction probability threshold (prediction (pred) > 0.5). Results from the two model trainings were integrated, sorted by count values in descending order. Furthermore, drugs with therapeutic potential shared by the two datasets were screened for molecular docking via CB-dock2 (https://cadd.labshare.cn/cb-dock2/php/index.php). Grid centers were automatically generated around protein active sites, and docking was performed with default parameters (binding energy < -5.0 kcal/mol).

2.11 Molecular dynamics simulation

Molecular dynamics simulations were performed using GROMACS software (v2024.4)(Fu et al. 2022) on the complex with the highest docking affinity for each prognostic gene. Parameters and topology files for the proteins (encoded by prognostic genes) and small-molecule ligands (drugs) were generated using the "AMBER14SB" force field and AMBER gaff force field, respectively. Periodic boundary conditions were set and optimized to define the size of the simulation box, which was then solvated with water molecules. To ensure electrical neutrality of the system, some solvent water molecules were replaced with Na^+ and Cl^- at a concentration of 0.15 mol/L. The steepest descent algorithm was used to minimize the energy of the entire system. Pre-equilibration was performed in two stages: the first stage involved NVT ensemble (with constant particle number, volume, and temperature) simulation at 300 K for 100 ps to stabilize the system temperature, and the second stage involved NPT ensemble (with constant particle number, pressure, and temperature) simulation at one bar for 100 ps to stabilize the system pressure. The computed parameters included: root-mean-square deviation (RMSD) of the protein-prognostic gene complex, root-mean-square fluctuation (RMSF) of the protein, total system energy, and number of hydrogen bonds formed.

2.12 Localization and targeted regulation of prognostic genes

We employed the RCircos package (v1.2.2)(Zhang et al. 2013) and integrated genome reference annotations (gencode.v19.annotation.gtf.gz) to generate a gene localization map, which visually illustrates the distribution of prognostic genes across chromosomes. The subcellular localization of prognostic genes was analyzed to provide a basis for understanding their biological functions and mechanisms of action. Furthermore, protein products encoded by prognostic genes were acquired from the UniProt database (https://www.uniprot.org/), along with their corresponding UniProt IDs and information on known functional domains. Subsequently, the types, names, and positions of functional domains of the proteins encoded by each gene were extracted, and conserved domains associated with functions such as signal transduction, DNA binding, and enzyme catalysis were identified for visualization. To achieve targeted regulation of prognostic genes, transcription factors (TFs) targeting

these genes were predicted using the CHEA3 database (https://maayanlab.cloud/chea3/). Additionally, miRNAs targeting the prognostic genes were retrieved from the miRDB database (https://mirdb.org/) and the miRNet database (https://www.mirnet.ca), with only the predicted results shared by both databases retained.

2.13 Statistical analysis

The R software (v4.2.2) was applied to conduct bioinformatics analysis. The Wilcoxon test was utilized to evaluate paired sample comparisons, with statistical significance defined as p value < 0.05. P value adjustment was performed for multiple comparisons as needed using the Benjamini-Hochberg (BH) method (for FDR control).

3. Results

3.1 The 129 druggable-signature genes with a significant causal relationship to KIRC

A sum of 1,768 DEGs were obtained from the TCGA-KIRC dataset. Compared with the control samples, the expression levels of 1,140 DEGs were markedly upregulated in KIRC samples, while 628 DEGs were downregulated (**Fig.1a**). The heatmap displayed that the top 20 DEGs with the largest absolute FC values (10 upregulated and 10 downregulated) exhibited distinct expression profiles between the KIRC and control samples, indicating marked transcriptional alterations (**Fig.1b**). Subsequently, based on 5,883 druggable genes, these genes were shared 838 genes with the DEGs, thus identifying 838 candidate genes (**Fig.1c**). After screening, 209 candidate genes and their corresponding 13,187 SNPs were retained for MR analysis (**Supplementary Table 2**). The IVW method showed that all candidate genes had a significant causal association with KIRC. Among them, 105 were risk factors (OR > 1; e.g., *HDAC10, SCNN1D, RAD54L, AMH, ASIC3, PLK1*) and 104 (e.g., *CDK3*, *BGLAP*, *DDIT4*, *FLRT1*, *ALDH6A1*) were protective factors for KIRC (OR < 1) (**Supplementary Table 3**). The assessment further illustrated the reliability and robustness of the MR results. Sensitivity analysis results showed that 187 candidate genes exhibited no heterogeneity (p > 0.05), while 22 candidate genes were analyzed using the random-effects model. Then, 146 candidate genes without horizontal pleiotropy (p > 0.05) were retained for further analyses (**Supplementary Table 4**). A causal relationship between 146 candidate genes and KIRC was validated (TRUE). Among these, the Steiger p values for 17 candidate genes were calculated as NA; thus, only 129 candidate genes were retained for subsequent analyses (TRUE, p < 0.0001) (**Supplementary Table 5**). For the visualization section, owing to space limitations, *ALDH6A1* was used as an example. Specifically, the scatter plot revealed that the intercepts of the five algorithms were around 0, indicating minimal influence from confounding factors. The slope of *ALDH6A1* was negative, confirming it as a protective factor for KIRC (**Fig. 1d**). Similarly, the SNP loci of *ALDH6A1* were located on the left side of the dashed line, which was consistent with the aforementioned result (**Fig.1e**). Furthermore, the SNPs of *ALDH6A1* showed an approximately symmetrical distribution on the left and right sides in the funnel plot, which was in line with the random grouping principle of Mendel's second law (**Fig.1f**). After sequentially

excluding each SNP of *ALDH6A1*, the effect of the remaining SNPs on the KIRC risk showed little change (**Fig.1g**). This suggested that the results had good stability and high reliability.

3.2 Functional characterization and interactions of candidate genes

Functional characterization demonstrated that 129 candidate genes were markedly enriched in pathways such as regulation of leukocyte mediated cytotoxicity, regulation of leukocyte proliferation, T cell proliferation, regulation of immune effector process, immunological synapse, chemokine activity (GO), ECM-receptor interaction, cytokine-cytokine receptor interaction, Th17 cell differentiation, PI3K/AKT signaling pathway, and JAK/STAT signaling pathway (KEGG) (adjusted p-value < 0.05) (**Fig.1h; Supplementary Table 6**). The significant enrichment of these functional terms indicates that the candidate genes were associated with core processes of KIRC, such as immune regulation, metabolic reprogramming, and invasion-metastasis. Moreover, in the protein-protein interaction (PPI) network, 98 candidate genes had complex interactions at the protein level, with 330 interaction pairs. For example, *CD86, CD80, PRF1, GZMB*, and *CD5* interacted with other candidate genes with a high degree at the protein level (**Fig.1i**).

3.3 Construction of a druggable signature-related prognostic risk model

A sum of 50 candidate genes were identified as markedly associated with the prognosis of KIRC, and 42 of these were risk factors for KIRC (HR > 1, p < 0.01) (**Fig.2a**). All 50 candidate genes satisfied the proportional hazards assumption (p > 0.05) (**Supplementary Table 7**). By integrating MR results, 28 genes with consistent associations with KIRC risk were identified, among which three were protective factors (*ABCB4, ALDH6A1, RGS5)* and 25 were risk factors (e.g., *AMH*, *ASIC3*, AURKB) (**Fig.2b**). LASSO regression analysis showed that the model performance was optimal at log(lambda.min) = -2.5508. At this point, the coefficients of *ALDH6A1*, *AMH*, *ASIC3*, and *PLK1* were not penalized to zero, with values of -0.160466585, 0.23855270834574, 0.119621320611586, and 0.465023176187918, respectively (**Fig.2c**). Subsequently, the high-risk (n = 199) and low-risk groups (n = 322) were classified according to the cutpoint (0.105356). Notably, KIRC samples in the high-risk group had markedly poorer survival outcomes (**Fig.2d**). This finding was further validated by the KM survival curve, which confirmed that KIRC samples in the high-risk group had a markedly lower survival rate (p < 0.0001) (**Fig.2e**). Ultimately, AUC values at the 1/2/3-year time points were all > 0.70, suggesting that the risk model exhibited favorable performance in predicting KIRC survival (**Fig.2f**). Additionally, compared with the low-risk group, *AMH*, *ASIC3*, and *PLK1* had higher relative expression in the high-risk group (**Fig.2g**), corresponding to the results of the univariate Cox regression and MR analyses. The generalizability of the KIRC risk model was further validated in the external validation set (**Fig.2h-k**). In summary, KIRC risk model (linked to druggable signatures via prognostic genes) exhibited favorable accuracy and generalizability in both internal and external validation, which provided a reliable basis for risk-stratified treatment of KIRC patients. Furthermore, there were marked differences in risk scores between subgroups stratified by different clinical indicators. Specifically, the risk score increased with the progression of KIRC (as per M, N, T, and stages). Notably, male patients had higher risk scores compared

to female patients, indicating that male patients were associated with a worse prognosis, which was consistent with current research findings(Hwang et al. 2024) (**Fig.3a, b**). These results further highlight the significance of risk score-based stratification for KIRC patients.

3.4 Risk score-altered pathway enrichment, immune microenvironment, and immunotherapy response in KIRC

There were 17,971 DEGs between the risk groups, which were significantly enriched in 41 pathways (**Supplementary Table 8**). These pathways mainly included cytokine-cytokine receptor interaction, chemokine signaling pathway, JAK/STAT signaling pathway, fatty acid metabolism, glycolysis/gluconeogenesis, and oxidative phosphorylation, suggesting that the druggable-related risk scores significantly alter the enrichment levels of pathways associated with KIRC pathology (**Fig.4a**). Furthermore, the infiltration patterns of 34 immune cells are shown in **Fig.4b**. 25 immune cells showed differential infiltration between the risk groups, among which only conventional dendritic cells, mast cells, naive $CD8^+$ T cells, neutrophils, and regulatory T cells exhibited higher infiltration in the low-risk group ($p < 0.05$). This suggested that the high-risk group might exhibit an immune-activated state (**Fig.4c**). Differentially infiltrated cells showed strong correlations, predominantly positive. For instance, effector memory $CD8^+$ T cells and $CD8^+$ T cells exhibited the strongest positive correlation (cor = 0.86), followed by the correlation between central memory $CD8^+$ T cells and $CD8^+$ T cells (cor = 0.85). In contrast, naive $CD8^+$ T cells only showed strong negative correlations with other cells, such as central memory $CD8^+$ T cells, gamma delta T cells, and macrophages (cor < -0.50) (**Fig.4d**). Notably, the relationship trend between differentially infiltrated immune cells and prognostic genes was consistent with the relationship between prognostic genes and KIRC risk. The protective factor *ALDH6A1* generally showed negative correlations with these cells, whereas *AMH*, *ASIC3*, *PLK1* (and risk score) exhibited largely opposite trends. For example, *ALDH6A1* had a strong negative correlation with T helper 1 cells (cor = -0.35), while *AMH*, *ASIC3*, *PLK1*, and risk score all showed strong positive correlations with T helper 1 cells (cor ≥ 0.35) (**Fig.4e**). Consistently, compared with the low-risk group, the high-risk group was associated with higher stromal scores ($p < 0.05$), ESTIMATE scores ($p < 0.0001$), and immune scores ($p < 0.0001$), as well as lower tumor purity ($p < 0.0001$). Among these, the risk score showed strong correlations with ESTIMATE scores (cor = 0.33), immune scores (cor = 0.41), and tumor purity (cor = -0.33) ($p < 0.0001$) (**Fig.4f**). Furthermore, compared with the low-risk group, the high-risk group was associated with higher levels of CAFs, $CD8^+$ T cells, dysfunction score, IFNG, MDSCs, Merck18, and TIDE score. This indicated that the tumor microenvironment of high-risk KIRC patients exhibited characteristics such as enhanced immune suppression and effector immune dysfunction, which might be accompanied by poorer treatment response and prognosis. In contrast, low-risk KIRC patients were associated with higher MSI and TAM M2 levels, which might be related to stronger immunogenicity, making tumor cells more susceptible to recognition and elimination by the immune system—this could also be one of the important reasons for their lower risk classification (**Fig.4g**). Furthermore, based on the TIDE score, KIRC patients showed an overall low response to immunotherapy. Specifically, the response rate was 43% in low-risk KIRC patients, compared with only 28% in high-risk patients (**Fig.4h**).

In summary, the druggable-related risk score can significantly affect the immune microenvironment and response to immunotherapy in KIRC patients, providing a basis for formulating immunotherapeutic strategies and thereby improving the benefits of immunotherapy for KIRC.

3.5 Druggability-related risk score effectively stratifying KIRC patients' somatic mutation rate

There were also differences in the somatic mutation rate between the risk groups. Specifically, the somatic mutation rate in the high-risk group (92.56%) was significantly higher than that in the low-risk group (85.84%). However, the mutation types were similar, with missense mutations being the most frequent. The gene with the highest mutation frequency was VHL in both groups, accounting for 45% in the high-risk group and 48% in the low-risk group. Frameshift deletions were another type of mutation with a relatively high frequency (**Fig.4i**). Correspondingly, the distribution of TMB was highly similar between the high-risk and low-risk groups, with the overall distribution ranging from 0 to 2.5 mutations/MB. The TMB in the high-risk group was higher than that in the low-risk group (**Fig.4j**). This provides data support for explaining the rationality of risk stratification at the molecular level and for subsequent optimization of therapeutic strategies based on mutation characteristics (e.g., TMB-guided immunotherapy).

3.6 Efficient prediction of high-probability small molecule-prognostic gene interaction pairs by the GraphBAN model

The GraphBAN model was trained using BindingDB and BioSNAP databases, and 66 shared drugs showed an interaction probability greater than 0.5 (**Supplementary Table 9**). Based on this, we matched four drugs with therapeutic potential from the literature, including fospropofol(Tang et al. 2024; Li et al. 2018) , taurine(Ma et al. 2022; Ping et al. 2023) , thiosulfuric acid(Meijer et al. 2024; Ng et al. 2003) , and zanamivir(Yang et al. 2024) , all of which are associated with more than two prognostic genes. Molecular docking results revealed that *ALDH6A1* has favorable binding affinities with fospropofol (CID_3038498; -6.6 kcal/mol) and zanamivir (CID_60855; -6.4 kcal/mol); *AMH* with fospropofol (CID_3038498; -6.5 kcal/mol); *ASIC3* with fospropofol (CID_3038498; -6.9 kcal/mol); and *PLK1* with zanamivir (CID_60855; -7.0 kcal/mol). These findings provide candidate genes for molecular targets in KIRC (**Fig.5a-e; Supplementary Table 10**). In the molecular dynamics, RMSD results showed that within 0-100 ns, the complexes with favorable binding affinities—*ALDH6A1*_fospropofol, *ALDH6A1*_zanamivir, *ASIC3*_fospropofol, and *PLK1*_zanamivir—exhibited minimal fluctuations, indicating stable binding between the small molecules and proteins. The *AMH*_fospropofol complex also remained relatively stable within 0-100 ns, with fluctuations observed between 75-85 ns (**Fig.6a**). RMSF results revealed that complexes formed with *ALDH6A1* displayed similar fluctuation trends in the 0-400 amino acid residue region, with small RMSF values ranging overall from 0.1-0.5 nm, suggesting these regions are relatively rigid and likely correspond to binding sites. Notably, RMSF values increased significantly after residue 400. For the *AMH*_fospropofol complex, overall RMSF fluctuations within 0-150 residues ranged from 0-0.6 nm, with significant fluctuations observed in the 25-50, 60-75, and 110-140 residue regions, potentially indicating flexible domains. The *ASIC3*_fospropofol complex showed small and stable RMSF

values in the 0-100 residue region, while *PLK1*_zanamivir exhibited small and stable RMSF values in the 0-250 residue region (**Fig.6b**). Additionally, throughout the simulation, the total energy of the complexes remained at a low level with a stable trend and minimal fluctuations (**Fig.6c**). Finally, the number of hydrogen bonds in *AMH*_fospropofol and *ASIC3*_fospropofol complexes showed little overall variation, generally remaining between 1-3. In contrast, hydrogen bond counts in *ALDH6A1*- and *PLK1*-related complexes fluctuated relatively more, ranging overall from 1-5 (**Fig.6d**). In summary, the docking results between the prognostic genes and these drugs were relatively stable, confirming the stability of the docking outcomes.

3.7 Molecular characteristics and regulatory networks of prognostic genes

Chromosomal localization analysis show that ASIC3, ALDH6A1, PLK1, and AMH are mapped to chromosomes 7, 14, 16, and 19, respectively (**Fig.7a**). Moreover, the distribution of prognostic genes was generally similar, with predominant localization in the cytosol, extracellular exosomes, and nucleus (score ≥ 0.396). Notably, PLK1 had the highest localization score in the cytosol (score = 0.816), while ALDH6A1 showed a high localization score in the endoplasmic reticulum (score = 0.695) (**Fig.7b**). The distribution of functional domains, modification sites, and specific functional elements on the amino acid sequences of proteins encoded by prognostic genes is shown in **Fig.7c**. Among them, PLK1_HUMAN, a key kinase in the cell cycle, has a domain distribution that intuitively explains its precise regulation of cell division: it phosphorylates substrates via kinase activity, recognizes targets through the POLO box, and is degraded in the late cell cycle via the D-box. Finally, we further elucidated the regulatory mechanisms of the prognostic genes. Specifically, 31, 81, 103, and 51 TFs target and regulate ALDH6A1, AMH, ASIC3, and PLK1, respectively, thereby forming a pre-transcriptional regulatory network comprising 266 regulatory axes. Among these, CTCF, E2F4, and MYC collectively target and regulate all four prognostic genes (**Fig.7d**). Similarly, based on the miRDB and miRNet databases, 36 shared miRNAs were obtained, with 26, 9, 2, and 22 miRNAs targeting and regulating ALDH6A1, AMH, ASIC3, and PLK1, respectively, involving 59 miRNA-mRNA regulatory pairs. Notably, hsa-miR-15a-5p and hsa-miR-15b-5p collectively target all four prognostic genes (**Fig.7e, f**). The revelation of this hierarchical regulatory network provides a basis for the targeted regulation of the prognostic genes.

4. Discussion

RCC is one of globally common malignant tumors, with KIRC as its most prevalent histopathological subtype(Xu et al. 2023; Zeng et al. 2022) . While surgical resection achieves favorable outcomes for early-stage KIRC patients, advanced and metastatic disease remains refractory to radiotherapy and chemotherapy, resulting in poor prognosis(Qin et al. 2019; Chen et al. 2022) . To address the unmet need for prognostic biomarkers and druggable targets, we integrated multiple bioinformatics approaches, including differential expression analysis of TCGA-KIRC data, MR, survival analysis, and LASSO regression, to systematically identify four prognostic genes (*ALDH6A1*, *AMH*, *ASIC3*, and *PLK1*) with significant causal associations with KIRC and "druggable" potential. The constructed risk model exhibited robust prognostic predictive performance (AUC > 0.7) and a positive correlation with tumor

pathological stage progression. Functional analyses revealed that the risk score markedly impacts the enrichment of key KIRC pathological pathways and effectively stratifies the TIME and immunotherapeutic response. Furthermore, using the GraphBAN model combined with molecular docking and molecular dynamics simulations, we confirmed that candidate drugs form stable complexes with target proteins, highlighting their potential as targets. This study provides novel candidate targets and a theoretical basis for KIRC risk stratification, immunotherapeutic strategy optimization, and targeted drug development.

Aldehyde dehydrogenase 6 family member A1 (*ALDH6A1*) encodes a mitochondrial aldehyde dehydrogenase involved in fatty acid metabolism and the catabolism of valine and thymine(Knebel et al. 2017) . Consistent with our findings, previous studies demonstrated significant downregulation of *ALDH6A1* in KIRC, with lower expression correlating negatively with patient survival(Guo et al. 2021; Lu et al. 2020) . *ALDH6A1* overexpression inhibits KIRC cell proliferation, migration, and metabolic reprogramming(Lu et al. 2020) , and it was included in a seven-gene prognostic signature enriched in tumorigenic and immune regulatory pathways, with the derived risk score predicting drug efficacy(Xia et al. 2023) . As a tumor suppressor with confirmed functional relevance in KIRC, *ALDH6A1* is a promising druggable target.

Anti-Müllerian hormone (*AMH*) encodes a dimeric glycoprotein of the transforming growth factor-β (TGF-β) superfamily. Recent studies revealed that its functional receptor *AMH*RII is widely expressed in multiple non-gynecologic solid tumors, implicating the *AMH* signaling pathway in diverse tumor biological processes and supporting its potential as a pan-cancer therapeutic target . A comparable study identified an 11-gene immune-related prognostic model (including *AMH*) that accurately predicts KIRC survival, with *AMH* highly expressed in high-risk patients, which is consistent with our results . The TGF-β superfamily regulates cell proliferation, differentiation, and immune suppression, suggesting *AMH* may promote KIRC progression through these pathways. Its high expression in high-risk groups and membership in a validated prognostic signature support its druggable potential and clinical relevance.

Acid-sensing ion channel 3 (*ASIC3*) belongs to the ASIC family, primarily expressed in the central and peripheral nervous systems. To our knowledge, this is the first report linking *ASIC3* to KIRC. Ion channel dysregulation is a key cancer hallmark, with membrane potential alterations influencing cell cycle, migration, and metabolism(Barret et al. 2021; Niklasson et al. 2017) . As a newly identified prognostic druggable gene in KIRC, *ASIC3* may contribute to tumorigenesis by disrupting ion homeostasis, warranting further functional validation.

Polo-like kinase 1 (*PLK1*), a conserved serine/threonine kinase, plays an indispensable role in the regulation of cell cycle processes, including spindle assembly, chromosome segregation and cytokinesis(Kalous et al. 2023) . Our findings are consistent with previous studies, in KIRC, *PLK1* expression is significantly upregulated, correlating with adverse clinical features, shortened disease-free/overall survival, and sunitinib resistance(Gao et al. 2020; Dufies et al. 2021) . Mechanistically, *PLK1* promotes KIRC proliferation and reduces apoptosis via minichromosome maintenance complex

component 3 (*MCM3*) phosphorylation, while its depletion inhibits tumor growth and metastasis(Gao et al. 2020) . Its confirmed druggability(Tan et al. 2025) and role in treatment resistance make it a high-priority therapeutic target.

The risk model (AUC > 0.7) constructed by integrating prognostic genes in our study effectively stratified KIRC patients by survival status, acting as a robust clinical tool for precision prognosis evaluation and individualized treatment planning. Accurate prediction of KIRC pathological grade is critical for optimizing treatment(Li et al. 2024) , and our finding of a positive correlation between risk score and T/N/M stage suggests the model could complement existing clinical parameters to enhance risk stratification. This allows clinicians to pinpoint high-risk patients who are likely to benefit from more intensive therapeutic interventions, thereby tackling the clinical dilemma posed by the heterogeneous outcomes of KIRC.

The risk score significantly altered the enrichment of pathways central to KIRC pathology, including cytokine-cytokine receptor interaction, chemokine signaling, JAK/STAT signaling, fatty acid metabolism, glycolysis/gluconeogenesis, and oxidative phosphorylation. Among them, Janus kinase/signal transducer and activator of transcription (JAK/STAT) signaling pathway plays a central role in cell proliferation, survival, differentiation, and immune responses. Early studies demonstrated that resistance to interferon-α (IFN-α), a historical immunotherapeutic agent for RCC, is associated with decreased expression of Jak1, Tyk2, and Stat1 proteins and impaired JAK/STAT pathway activation(Shang et al. 2007) . Restoring Jak or Stat1 expression significantly enhances RCC sensitivity to IFN-α, highlighting the pathway's potential as a therapeutic target. More recently, EH domain-binding protein 1-like 1 (EHBP1L1) was identified as a key mediator of the IFN-γ/JAK1/STAT1/PD-L1 pathway in RCC, interacting with JAK1 to maintain its stability and competing with SOCS1 for JAK1 binding(Pan et al. 2023) . This interaction increases JAK1 protein levels and enhances JAK1/STAT1/PD-L1 pathway activity, fostering an immunosuppressive TIME. Combining EHBP1L1 inhibition with immune checkpoint blockade (ICB) reshapes the immunosuppressive TIME, prevents tumor immune escape, and significantly improves ICB efficacy(Pan et al. 2023) . These EHBP1L1-related findings, together with our pathway enrichment results, suggest that targeting JAK/STAT and other dysregulated pathways may interfere with KIRC progression—a hypothesis supported by recent preclinical studies(Deng et al. 2023; Chen et al. 2025) . Beyond immune pathways, our analyses reveal marked metabolic alterations. Metabolic reprogramming is a well-recognized hallmark of KIRC, with dysregulated fatty acid metabolism, glycolysis, and oxidative phosphorylation contribute to tumor growth and survival(Lucarelli et al. 2019; Wolf et al. 2020) . Our identification of these metabolic pathways as enriched in high-risk patients aligns with KIRC's classification as a metabolic disease and underscores the role of the prognostic druggable genes in regulating metabolic homeostasis. For instance, *ALDH6A1*'s involvement in fatty acid metabolism may link its downregulation to metabolic derangement in KIRC. Thus, the targeting of these metabolic pathways or the regulation of validated prognostic druggable genes represents a viable therapeutic strategy for KIRC, which is worthy of additional experimental investigation.

As a key regulator of KIRC progression and treatment outcomes, the tumor immune microenvironment (TIME) relies on immune cell infiltration as a critical factor governing the efficacy of immunotherapeutic regimens(Su et al. 2021) . Immune infiltration analysis identified 25 differentially infiltrated immune cells, with most enriched in high-risk groups. T cells are central to KIRC TIME: $CD8^+$ T cells mediate tumor killing, while $CD4^+$ T cell function depends on polarization(Siska et al. 2015; Bronte et al. 2016) . In our study, compared to low-risk groups, high-risk KIRC patients exhibited higher $CD8^+$ T cell infiltration yet lower predicted immunotherapy response, consistent with reported immunosuppressive TIME(Su et al. 2021) . Further analysis confirmed CAFs/MDSCs enrichment and increased immune exclusion/T cell dysfunction scores in high-risk patients(Gandellini et al. 2015; Hakimi et al. 2019) , fostering tumor immune evasion. Of note, this is the first study to associate four prognostic druggable genes (*ALDH6A1*, *AMH*, *ASIC3*, *PLK1*) and the integrated risk score with these inhibitory indices, implying their involvement in TIME remodeling.

Overall, the risk model achieves effective prognostic stratification and uncovers immunological bases for adverse outcomes in high-risk patients. $CD8^+$ T cell infiltration alone is insufficient for immunotherapeutic prediction; thorough evaluation of inhibitory TIME components is imperative. High-risk patients may require combination strategies to reverse immunosuppression. The identified druggable genes represent promising targets for TIME regulation, providing new insights into personalized combinatorial immunotherapy for KIRC.

Using the GraphBAN model, we predicted candidate compounds targeting the four prognostic genes, including fospropofol, taurine, thiosulfate and zanamivir. Fospropofol exhibited robust binding affinities (≤ -6.5 kcal/mol) to *ALDH6A1*, *AMH* and *ASIC3*, and zanamivir to *PLK1*. Molecular dynamics simulations verified the binding stability of these complexes. Fospropofol, a prodrug of intravenous anesthetic propofol, is metabolized to active propofol in vivo. Previous studies showed propofol exerts potent antitumor activity in multiple cancers; in clear cell renal cell carcinoma (ccRCC), it disrupts tumorigenesis via the circFBXW7/miR-942 axis(Huang et al. 2022) , regulates HIF-1α by targeting SIRT1 pathway(Chen et al. 2023) , and inhibits cancer cell proliferation, migration, invasion and EMT via miR-363/Snail1 axis(Shi et al. 2021) . These findings indicate propofol and its prodrug fospropofol may inhibit KIRC progression via multi-targeted, multi-pathway actions. Our study predicted and validated fospropofol's binding to three prognostic genes (*ALDH6A1*, *AMH*, *ASIC3*): *ALDH6A1* (key metabolic enzyme), *AMH* (TGF-β superfamily signaling) and *ASIC3* (ion channel regulator). Fospropofol's binding to these functionally distinct proteins suggests anti-KIRC effects via metabolic reprogramming, growth factor signaling and membrane potential homeostasis. Taurine is a differential metabolite in RCC(Huynh et al. 2023; Jimenez-Alonso et al. 2023) , while zanamivir exhibits anti-tumor activity in gastric cancer with favorable renal safety(Altschuler et al. 2005; Yang et al. 2024) , providing a preliminary safety rationale for KIRC. Taken together, GraphBAN-based prediction and validation link two clinically approved drugs (fospropofol, zanamivir) to novel KIRC prognostic targets, elucidating their potential mechanisms and enabling new drug repurposing for KIRC targeted therapy.

This study has some limitations. First, it relies on public TCGA-KIRC data, which has inherent biases. Additionally, mechanistic insights remain preliminary due to the lack of experimental validation. Furthermore, clinical validation of the risk model and candidate compounds is required. Future research will validate gene functions in vitro/in vivo, refine the model by integrating clinical parameters and multi-center cohort data, and evaluate candidate compound efficacy in combination with existing therapies. We will also explore the synergistic interactions within the core gene network to deepen understanding of their role in KIRC progression.

5. Conclusion

In summary, we identified four druggable prognostic genes in KIRC via integrated bioinformatics analyses, constructing a robust risk model correlated with pathological stage. The risk score modulates key oncogenic pathways and immune infiltration, predicting immunotherapeutic response. Candidate drugs with stable target binding were identified, supporting their translational potential. Our findings highlights a core gene network that drives KIRC progression through metabolic and immune dysregulation. Despite limitations, this study advances precision medicine in KIRC, providing novel biomarkers, therapeutic targets, and a theoretical basis for improving diagnosis and treatment outcomes.

Declarations

Author Contributions: X. Deng, H. Zhang, and T. Zhang conceived and designed the research; Y. Lu analyzed and interpreted the data. All authors were involved in drafting and revising the manuscript. The authors declare that all data were generated in-house, that no paper mill was used and that no AI tool has been used for the generation of text or figures.

Funding: This research was funded by Guangzhou Science and Technology Program Project, Guangzhou Youth Medical Innovation and Practice Research Program (Oncology Field), and Guangzhou Health Science and Technology General Guidance Program, grant number 2025A03J3386, 2023QNYXYB013 and 20261A011015. The APC was funded by Guangzhou Science and Technology Program Project.

Institutional Review Board Statement: As this research did not utilize any samples derived from animal or human participants, no ethical review and approval were necessary.

Informed Consent Statement: Not applicable.

Clinical trial number: Not applicable.

Data Availability Statement: All data supporting the findings of this study are publicly available. The transcriptomic and clinical data for kidney renal clear cell carcinoma (TCGA-KIRC) were obtained from The Cancer Genome Atlas portal (https://portal.gdc.cancer.gov). The ArrayExpress dataset E-MTAB-1980 is accessible at https://www.ebi.ac.uk/biostudies/arrayexpress/studies/E-MTAB-1980. Summary

statistics for kidney clear cell carcinoma (Release 12) were sourced from the FinnGen consortium (https://r12.finngen.fi). The druggable gene list was compiled from the Drug-Gene Interaction Database (DGIdb v4.2.0, https://www.dgidb.org) and complementary published literature. All data were accessed on July 23, 2025. No new primary data were generated in this study.

Conflicts of Interest: The authors declare no conflicts of interest.

References

1. Altschuler, E. L., Bhatia, A. & Kast, R. E. (2005) Consideration of use of neuraminidase inhibitors such as oseltamivir and zanamivir in IgA nephropathy. *Kidney Int,* 68**,** 2910-1. https://doi.org/10.1111/j.1523-1755.2005.00583_7.x
2. Barret, J. M., Nicolas, A., Jarry, A., Dubreuil, O., Meseure, D., Passat, T., et al. (2021) The Expression of Anti-Mullerian Hormone Type II Receptor (AMHRII) in Non-Gynecological Solid Tumors Offers Potential for Broad Therapeutic Intervention in Cancer. *Biology (Basel),* 10. https://doi.org/10.3390/biology10040305
3. Berquist, S. W., Yim, K., Ryan, S. T., Patel, S. H., Eldefrawy, A., Cotta, B. H., et al. (2019) Systemic therapy in the management of localized and locally advanced renal cell carcinoma: Current state and future perspectives. *Int J Urol,* 26**,** 532-542. https://doi.org/10.1111/iju.13943
4. Bex, A., Albiges, L., Ljungberg, B., Bensalah, K., Dabestani, S., Giles, R. H., et al. (2018) Updated European Association of Urology Guidelines for Cytoreductive Nephrectomy in Patients with Synchronous Metastatic Clear-cell Renal Cell Carcinoma. *Eur Urol,* 74**,** 805-809. https://doi.org/10.1016/j.eururo.2018.08.008
5. Bowden, J., Davey Smith, G. & Burgess, S. (2015) Mendelian randomization with invalid instruments: effect estimation and bias detection through Egger regression. *Int J Epidemiol,* 44**,** 512-25. https://doi.org/10.1093/ije/dyv080
6. Bowden, J., Davey Smith, G., Haycock, P. C. & Burgess, S. (2016) Consistent Estimation in Mendelian Randomization with Some Invalid Instruments Using a Weighted Median Estimator. *Genet Epidemiol,* 40**,** 304-14. https://doi.org/10.1002/gepi.21965
7. Bronte, V., Brandau, S., Chen, S. H., Colombo, M. P., Frey, A. B., Greten, T. F., et al. (2016) Recommendations for myeloid-derived suppressor cell nomenclature and characterization standards. *Nat Commun,* 7**,** 12150. https://doi.org/10.1038/ncomms12150
8. Bukavina, L., Bensalah, K., Bray, F., Carlo, M., Challacombe, B., Karam, J. A., et al. (2022) Epidemiology of Renal Cell Carcinoma: 2022 Update. *Eur Urol,* 82**,** 529-542. https://doi.org/10.1016/j.eururo.2022.08.019
9. Burgess, S., Scott, R. A., Timpson, N. J., Davey Smith, G., Thompson, S. G. & Consortium, E.-I. (2015) Using published data in Mendelian randomization: a blueprint for efficient identification of causal risk factors. *Eur J Epidemiol,* 30**,** 543-52. https://doi.org/10.1007/s10654-015-0011-z

10. Cancer Genome Atlas Research, N. (2013) Comprehensive molecular characterization of clear cell renal cell carcinoma. *Nature,* 499**,** 43-9. https://doi.org/10.1038/nature12222
11. Chen, C., Yang, R. X., Zhang, J. X. & Xu, H. G. (2022) Construction and validation of a prognostic model for kidney renal clear cell carcinoma based on podocyte-associated genes. *Cancer Med,* 11**,** 3549-3562. https://doi.org/10.1002/cam4.4733
12. Chen, P., Yang, J., Chen, L., Liu, C., Li, Z., Long, X., et al. (2025) Moscatilin Induces Ferroptosis in Clear Cell Renal Cell Carcinoma via the JAK-STAT Signaling Pathway. *Chem Biol Drug Des,* 105**,** e70071. https://doi.org/10.1111/cbdd.70071
13. Chen, X., Li, C., Zeng, R., Qiu, L., Huang, J., Wang, N., et al. (2023) Propofol Regulates HIF-1 alpha Effect of Expression of Targeted SIRT1 Signal pathway on Kidney Renal Clear Cell Carcinoma. *Cell Mol Biol (Noisy-le-grand),* 69**,** 145-149. https://doi.org/10.14715/cmb/2023.69.3.21
14. Chen, Y., Xie, Y., Ci, H., Cheng, Z., Kuang, Y., Li, S., et al. (2024) Plasma metabolites and risk of seven cancers: a two-sample Mendelian randomization study among European descendants. *BMC Med,* 22**,** 90. https://doi.org/10.1186/s12916-024-03272-8
15. Damayanti, N. P., Cordova, R. A., Rupert, C., Delle Fontane, I., Shen, L., Orsi, S., et al. (2024) TFE3-Splicing Factor Fusions Represent Functional Drivers and Druggable Targets in Translocation Renal Cell Carcinoma. *Cancer Res,* 84**,** 1286-1302. https://doi.org/10.1158/0008-5472.CAN-23-1789
16. Deng, H., Gong, X., Ji, G., Li, C. & Cheng, S. (2023) KIF2C promotes clear cell renal cell carcinoma progression via activating JAK2/STAT3 signaling pathway. *Mol Cell Probes,* 72**,** 101938. https://doi.org/10.1016/j.mcp.2023.101938
17. Dufies, M., Verbiest, A., Cooley, L. S., Ndiaye, P. D., He, X., Nottet, N., et al. (2021) Plk1, upregulated by HIF-2, mediates metastasis and drug resistance of clear cell renal cell carcinoma. *Commun Biol,* 4**,** 166. https://doi.org/10.1038/s42003-021-01653-w
18. Emdin, C. A., Khera, A. V. & Kathiresan, S. (2017) Mendelian Randomization. *Jama,* 318**,** 1925-1926. https://doi.org/10.1001/jama.2017.17219
19. Engebretsen, S. & Bohlin, J. (2019) Statistical predictions with glmnet. *Clin Epigenetics,* 11**,** 123. https://doi.org/10.1186/s13148-019-0730-1
20. Finan, C., Gaulton, A., Kruger, F. A., Lumbers, R. T., Shah, T., Engmann, J., et al. (2017) The druggable genome and support for target identification and validation in drug development. *Sci Transl Med,* 9. https://doi.org/10.1126/scitranslmed.aag1166
21. Fu, S., Zhou, Y., Hu, C., Xu, Z. & Hou, J. (2022) Network pharmacology and molecular docking technology-based predictive study of the active ingredients and potential targets of rhubarb for the treatment of diabetic nephropathy. *BMC Complement Med Ther,* 22**,** 210. https://doi.org/10.1186/s12906-022-03662-6
22. Gandellini, P., Andriani, F., Merlino, G., D'Aiuto, F., Roz, L. & Callari, M. (2015) Complexity in the tumour microenvironment: Cancer associated fibroblast gene expression patterns identify both common and unique features of tumour-stroma crosstalk across cancer types. *Semin Cancer Biol,* 35**,** 96-106. https://doi.org/10.1016/j.semcancer.2015.08.008

23. Gao, Z., Man, X., Li, Z., Bi, J., Liu, X., Li, Z., et al. (2020) PLK1 promotes proliferation and suppresses apoptosis of renal cell carcinoma cells by phosphorylating MCM3. *Cancer Gene Ther,* 27**,** 412-423. https://doi.org/10.1038/s41417-019-0094-x
24. Guo, X., Sun, Z., Jiang, S., Jin, X. & Wang, H. (2021) Identification and validation of a two-gene metabolic signature for survival prediction in patients with kidney renal clear cell carcinoma. *Aging (Albany NY),* 13**,** 8276-8289. https://doi.org/10.18632/aging.202636
25. Hakimi, A. A., Voss, M. H., Kuo, F., Sanchez, A., Liu, M., Nixon, B. G., et al. (2019) Transcriptomic Profiling of the Tumor Microenvironment Reveals Distinct Subgroups of Clear Cell Renal Cell Cancer: Data from a Randomized Phase III Trial. *Cancer Discov,* 9**,** 510-525. https://doi.org/10.1158/2159-8290.CD-18-0957
26. Hartwig, F. P., Davey Smith, G. & Bowden, J. (2017) Robust inference in summary data Mendelian randomization via the zero modal pleiotropy assumption. *Int J Epidemiol,* 46**,** 1985-1998. https://doi.org/10.1093/ije/dyx102
27. Hemani, G., Zheng, J., Elsworth, B., Wade, K. H., Haberland, V., Baird, D., et al. (2018) The MR-Base platform supports systematic causal inference across the human phenome. *Elife,* 7. https://doi.org/10.7554/eLife.34408
28. Huang, Y., Wu, Y. & Lu, S. (2022) Propofol Disrupts Clear Cell Renal Cell Carcinoma Tumorigenesis by Regulating circFBXW7/miR-942 Axis. *Nephron,* 146**,** 514-527. https://doi.org/10.1159/000522285
29. Huynh, M. J., Gusev, A., Palmas, F., Vandergrift, L., Berker, Y., Wu, C. L., et al. (2023) Characterization of the metabolomic profile of renal cell carcinoma by high resolution magic angle spinning proton magnetic resonance spectroscopy. *Urol Oncol,* 41**,** 459 e9-459 e16. https://doi.org/10.1016/j.urolonc.2023.09.005
30. Hwang, J., Lee, H. E., Han, J. S., Choi, M. H., Hong, S. H., Kim, S. W., et al. (2024) Sex-specific survival gene mutations are discovered as clinical predictors of clear cell renal cell carcinoma. *Sci Rep,* 14**,** 15800. https://doi.org/10.1038/s41598-024-66525-9
31. Jimenez-Alonso, J. J., Guillen-Mancina, E., Calderon-Montano, J. M., Jimenez-Gonzalez, V., Diaz-Ortega, P., Burgos-Moron, E., et al. (2023) Artificial Diets with Altered Levels of Sulfur Amino Acids Induce Anticancer Activity in Mice with Metastatic Colon Cancer, Ovarian Cancer and Renal Cell Carcinoma. *Int J Mol Sci,* 24. https://doi.org/10.3390/ijms24054587
32. Kalous, J. & Aleshkina, D. (2023) Multiple Roles of PLK1 in Mitosis and Meiosis. *Cells,* 12. https://doi.org/10.3390/cells12010187
33. Knebel, B., Goeddeke, S., Poschmann, G., Markgraf, D. F., Jacob, S., Nitzgen, U., et al. (2017) Novel Insights into the Adipokinome of Obese and Obese/Diabetic Mouse Models. *Int J Mol Sci,* 18. https://doi.org/10.3390/ijms18091928
34. Kuzuoglu-Ozturk, D., Hu, Z., Rama, M., Devericks, E., Weiss, J., Chiang, G. G., et al. (2021) Revealing molecular pathways for cancer cell fitness through a genetic screen of the cancer translatome. *Cell Rep,* 35**,** 109321. https://doi.org/10.1016/j.celrep.2021.109321

35. Lasorsa, F., di Meo, N. A., Rutigliano, M., Milella, M., Ferro, M., Pandolfo, S. D., et al. (2023) Immune Checkpoint Inhibitors in Renal Cell Carcinoma: Molecular Basis and Rationale for Their Use in Clinical Practice. *Biomedicines,* 11. https://doi.org/10.3390/biomedicines11041071
36. Lei, J., Qu, T., Cha, L., Tian, L., Qiu, F., Guo, W., et al. (2023) Clinicopathological characteristics of pheochromocytoma/paraganglioma and screening of prognostic markers. *J Surg Oncol,* 128**,** 510-518. https://doi.org/10.1002/jso.27358
37. Li, R., Liu, H., Dilger, J. P. & Lin, J. (2018) Effect of Propofol on breast Cancer cell, the immune system, and patient outcome. *BMC Anesthesiol,* 18**,** 77. https://doi.org/10.1186/s12871-018-0543-3
38. Li, S., Zhou, Z., Gao, M., Liao, Z., He, K., Qu, W., et al. (2024) Incremental value of automatically segmented perirenal adipose tissue for pathological grading of clear cell renal cell carcinoma: a multicenter cohort study. *Int J Surg,* 110**,** 4221-4230. https://doi.org/10.1097/JS9.0000000000001358
39. Lin, L., Tang, Y., Ning, K., Li, X. & Hu, X. (2024) Investigating the causal associations between metabolic biomarkers and the risk of kidney cancer. *Commun Biol,* 7**,** 398. https://doi.org/10.1038/s42003-024-06114-8
40. Love, M. I., Huber, W. & Anders, S. (2014) Moderated estimation of fold change and dispersion for RNA-seq data with DESeq2. *Genome Biol,* 15**,** 550. https://doi.org/10.1186/s13059-014-0550-8
41. Lu, J., Chen, Z., Zhao, H., Dong, H., Zhu, L., Zhang, Y., et al. (2020) ABAT and ALDH6A1, regulated by transcription factor HNF4A, suppress tumorigenic capability in clear cell renal cell carcinoma. *J Transl Med,* 18**,** 101. https://doi.org/10.1186/s12967-020-02268-1
42. Lucarelli, G., Loizzo, D., Franzin, R., Battaglia, S., Ferro, M., Cantiello, F., et al. (2019) Metabolomic insights into pathophysiological mechanisms and biomarker discovery in clear cell renal cell carcinoma. *Expert Rev Mol Diagn,* 19**,** 397-407. https://doi.org/10.1080/14737159.2019.1607729
43. Ma, N., He, F., Kawanokuchi, J., Wang, G. & Yamashita, T. (2022) Taurine and Its Anticancer Functions: In Vivo and In Vitro Study. *Adv Exp Med Biol,* 1370**,** 121-128. https://doi.org/10.1007/978-3-030-93337-1_11
44. Meijer, A. J. M., Diepstraten, F. A., Ansari, M., Bouffet, E., Bleyer, A., Fresneau, B., et al. (2024) Use of Sodium Thiosulfate as an Otoprotectant in Patients With Cancer Treated With Platinum Compounds: A Review of the Literature. *J Clin Oncol,* 42**,** 2219-2232. https://doi.org/10.1200/JCO.23.02353
45. Nezami, B. G. & MacLennan, G. T. (2025) Clear Cell Renal Cell Carcinoma: A Comprehensive Review of its Histopathology, Genetics, and Differential Diagnosis. *Int J Surg Pathol,* 33**,** 265-280. https://doi.org/10.1177/10668969241256111
46. Ng, K. H., Lim, B. G. & Wong, K. P. (2003) Sulfate conjugating and transport functions of MDCK distal tubular cells. *Kidney Int,* 63**,** 976-86. https://doi.org/10.1046/j.1523-1755.2003.00818.x
47. Niklasson, M., Maddalo, G., Sramkova, Z., Mutlu, E., Wee, S., Sekyrova, P., et al. (2017) Membrane-Depolarizing Channel Blockers Induce Selective Glioma Cell Death by Impairing Nutrient Transport and Unfolded Protein/Amino Acid Responses. *Cancer Res,* 77**,** 1741-1752. https://doi.org/10.1158/0008-5472.CAN-16-2274

48. Pan, Y., Shu, G., Fu, L., Huang, K., Zhou, X., Gui, C., et al. (2023) EHBP1L1 Drives Immune Evasion in Renal Cell Carcinoma through Binding and Stabilizing JAK1. *Adv Sci (Weinh),* 10**,** e2206792. https://doi.org/10.1002/advs.202206792
49. Patergnani, S., Guzzo, S., Mangolini, A., dell'Atti, L., Pinton, P. & Aguiari, G. (2020) The induction of AMPK-dependent autophagy leads to P53 degradation and affects cell growth and migration in kidney cancer cells. *Exp Cell Res,* 395**,** 112190. https://doi.org/10.1016/j.yexcr.2020.112190
50. Ping, Y., Shan, J., Liu, Y., Liu, F., Wang, L., Liu, Z., et al. (2023) Taurine enhances the antitumor efficacy of PD-1 antibody by boosting CD8(+) T cell function. *Cancer Immunol Immunother,* 72**,** 1015-1027. https://doi.org/10.1007/s00262-022-03308-z
51. Posadas, E. M., Limvorasak, S., Sharma, S. & Figlin, R. A. (2013) Targeting angiogenesis in renal cell carcinoma. *Expert Opin Pharmacother,* 14**,** 2221-36. https://doi.org/10.1517/14656566.2013.832202
52. Qin, S., Shi, X., Wang, C., Jin, P. & Ma, F. (2019) Transcription Factor and miRNA Interplays Can Manifest the Survival of ccRCC Patients. *Cancers (Basel),* 11. https://doi.org/10.3390/cancers11111668
53. Radenbaugh, A. J., Ma, S., Ewing, A., Stuart, J. M., Collisson, E. A., Zhu, J., et al. (2014) RADIA: RNA and DNA integrated analysis for somatic mutation detection. *PLoS One,* 9**,** e111516. https://doi.org/10.1371/journal.pone.0111516
54. Robin, X., Turck, N., Hainard, A., Tiberti, N., Lisacek, F., Sanchez, J. C., et al. (2011) pROC: an open-source package for R and S+ to analyze and compare ROC curves. *BMC Bioinformatics,* 12**,** 77. https://doi.org/10.1186/1471-2105-12-77
55. Rustum, Y. M., Reis, R. & Rustum, T. M. (2023) Druggable Biomarkers Altered in Clear Cell Renal Cell Carcinoma: Strategy for the Development of Mechanism-Based Combination Therapy. *Int J Mol Sci,* 24. https://doi.org/10.3390/ijms24020902
56. Rysz, J., Franczyk, B., Lawinski, J. & Gluba-Brzozka, A. (2021) Characteristics of Clear Cell Papillary Renal Cell Carcinoma (ccpRCC). *Int J Mol Sci,* 23. https://doi.org/10.3390/ijms23010151
57. Shang, D., Liu, Y., Ito, N., Kamoto, T. & Ogawa, O. (2007) Defective Jak-Stat activation in renal cell carcinoma is associated with interferon-alpha resistance. *Cancer Sci,* 98**,** 1259-64. https://doi.org/10.1111/j.1349-7006.2007.00526.x
58. Shi, H., Yan, C., Chen, Y., Wang, Z., Guo, J. & Pei, H. (2021) Propofol inhibits the proliferation, migration, invasion and epithelial to mesenchymal transition of renal cell carcinoma cells by regulating microRNA-363/Snail1. *Am J Transl Res,* 13**,** 2256-2269.
59. Siska, P. J. & Rathmell, J. C. (2015) T cell metabolic fitness in antitumor immunity. *Trends Immunol,* 36**,** 257-64. https://doi.org/10.1016/j.it.2015.02.007
60. Su, S., Akbarinejad, S. & Shahriyari, L. (2021) Immune classification of clear cell renal cell carcinoma. *Sci Rep,* 11**,** 4338. https://doi.org/10.1038/s41598-021-83767-z
61. Tan, H. T., Ma, C. Y., Sun, C. H., Sun, S. Z., Zhang, M. X. & Wang, J. F. (2025) A novel programmed cell death signature predicts clinical outcomes in clear cell renal cell carcinoma and identifies PLK1 as a therapeutic target. *Apoptosis,* 30**,** 1797-1825. https://doi.org/10.1007/s10495-025-02126-9

62. Tang, Y., Tang, L., Yao, Y., Huang, H. & Chen, B. (2024) Effects of anesthesia on long-term survival in cancer surgery: A systematic review and meta-analysis. *Heliyon,* 10**,** e24791. https://doi.org/10.1016/j.heliyon.2024.e24791
63. Tao, S., Lin, Y., Huang, S., Lin, S., Jin, K. & Chen, H. (2023) Circulating inflammatory cytokines in relation to the risk of renal cell carcinoma: A gender-specific two-sample Mendelian randomization study. *Cancer Med,* 12**,** 21013-21021. https://doi.org/10.1002/cam4.6658
64. van den Heuvel, C., van Ewijk, A., Zeelen, C., de Bitter, T., Huynen, M., Mulders, P., et al. (2019) Molecular Profiling of Druggable Targets in Clear Cell Renal Cell Carcinoma Through Targeted RNA Sequencing. *Front Oncol,* 9**,** 117. https://doi.org/10.3389/fonc.2019.00117
65. Wolf, M. M., Kimryn Rathmell, W. & Beckermann, K. E. (2020) Modeling clear cell renal cell carcinoma and therapeutic implications. *Oncogene,* 39**,** 3413-3426. https://doi.org/10.1038/s41388-020-1234-3
66. Xia, G., Wu, S. & Cui, X. (2023) An immune infiltration-related prognostic model of kidney renal clear cell carcinoma with two valuable markers: CAPN12 and MSC. *Front Oncol,* 13**,** 1161666. https://doi.org/10.3389/fonc.2023.1161666
67. Xiong, W., Zhong, J., Li, Y., Li, X., Wu, L. & Zhang, L. (2022) Identification of Pathologic Grading-Related Genes Associated with Kidney Renal Clear Cell Carcinoma. *J Immunol Res,* 2022**,** 2818777. https://doi.org/10.1155/2022/2818777
68. Xu, T., Wei, D., Yang, Z., Xie, S., Yan, Z., Chen, C., et al. (2023) ApoM suppresses kidney renal clear cell carcinoma growth and metastasis via the Hippo-YAP signaling pathway. *Arch Biochem Biophys,* 743**,** 109642. https://doi.org/10.1016/j.abb.2023.109642
69. Yang, H., Li, Q., Chen, X., Weng, M., Huang, Y., Chen, Q., et al. (2024) Targeting SOX13 inhibits assembly of respiratory chain supercomplexes to overcome ferroptosis resistance in gastric cancer. *Nat Commun,* 15**,** 4296. https://doi.org/10.1038/s41467-024-48307-z
70. Yang, M., Wan, X., Zheng, H., Xu, K., Xie, J., Yu, H., et al. (2023) No Evidence of a Genetic Causal Relationship between Ankylosing Spondylitis and Gut Microbiota: A Two-Sample Mendelian Randomization Study. *Nutrients,* 15. https://doi.org/10.3390/nu15041057
71. Yoshihara, K., Shahmoradgoli, M., Martínez, E., Vegesna, R., Kim, H., Torres-Garcia, W., et al. (2013) Inferring tumour purity and stromal and immune cell admixture from expression data. *Nat Commun,* 4**,** 2612. https://doi.org/10.1038/ncomms3612
72. Yu, G., Wang, L. G., Han, Y. & He, Q. Y. (2012) clusterProfiler: an R package for comparing biological themes among gene clusters. *Omics,* 16**,** 284-7. https://doi.org/10.1089/omi.2011.0118
73. Zeng, D., Ye, Z., Shen, R., Yu, G., Wu, J., Xiong, Y., et al. (2021) IOBR: Multi-Omics Immuno-Oncology Biological Research to Decode Tumor Microenvironment and Signatures. *Front Immunol,* 12**,** 687975. https://doi.org/10.3389/fimmu.2021.687975
74. Zeng, W., Xiong, G., Hua, L., Hu, Y., Guo, X. & Peng, X. (2022) APOA1 mRNA and protein in kidney renal clear cell carcinoma correlate with the disease outcome. *Sci Rep,* 12**,** 12406. https://doi.org/10.1038/s41598-022-16434-6

75. Zhang, H., Meltzer, P. & Davis, S. (2013) RCircos: an R package for Circos 2D track plots. *BMC Bioinformatics,* 14**,** 244. https://doi.org/10.1186/1471-2105-14-244
76. Zhang, X., Wang, Z., Zeng, Z., Shen, N., Wang, B., Zhang, Y., et al. (2021) Bioinformatic analysis identifying FGF1 gene as a new prognostic indicator in clear cell Renal Cell Carcinoma. *Cancer Cell Int,* 21**,** 222. https://doi.org/10.1186/s12935-021-01917-9
77. Zheng, X., Wang, Y. & Qiu, X. (2024) Comprehensive analysis of MAPK genes in the prognosis, immune characteristics, and drug treatment of renal clear cell carcinoma using bioinformatic analysis and Mendelian randomization. *Eur J Pharmacol,* 980**,** 176840. https://doi.org/10.1016/j.ejphar.2024.176840
78. Zheng, Y., Gao, W., Zhang, Q., Cheng, X., Liu, Y., Qi, Z., et al. (2022) Ferroptosis and Autophagy-Related Genes in the Pathogenesis of Ischemic Cardiomyopathy. *Front Cardiovasc Med,* 9**,** 906753. https://doi.org/10.3389/fcvm.2022.906753

Figures

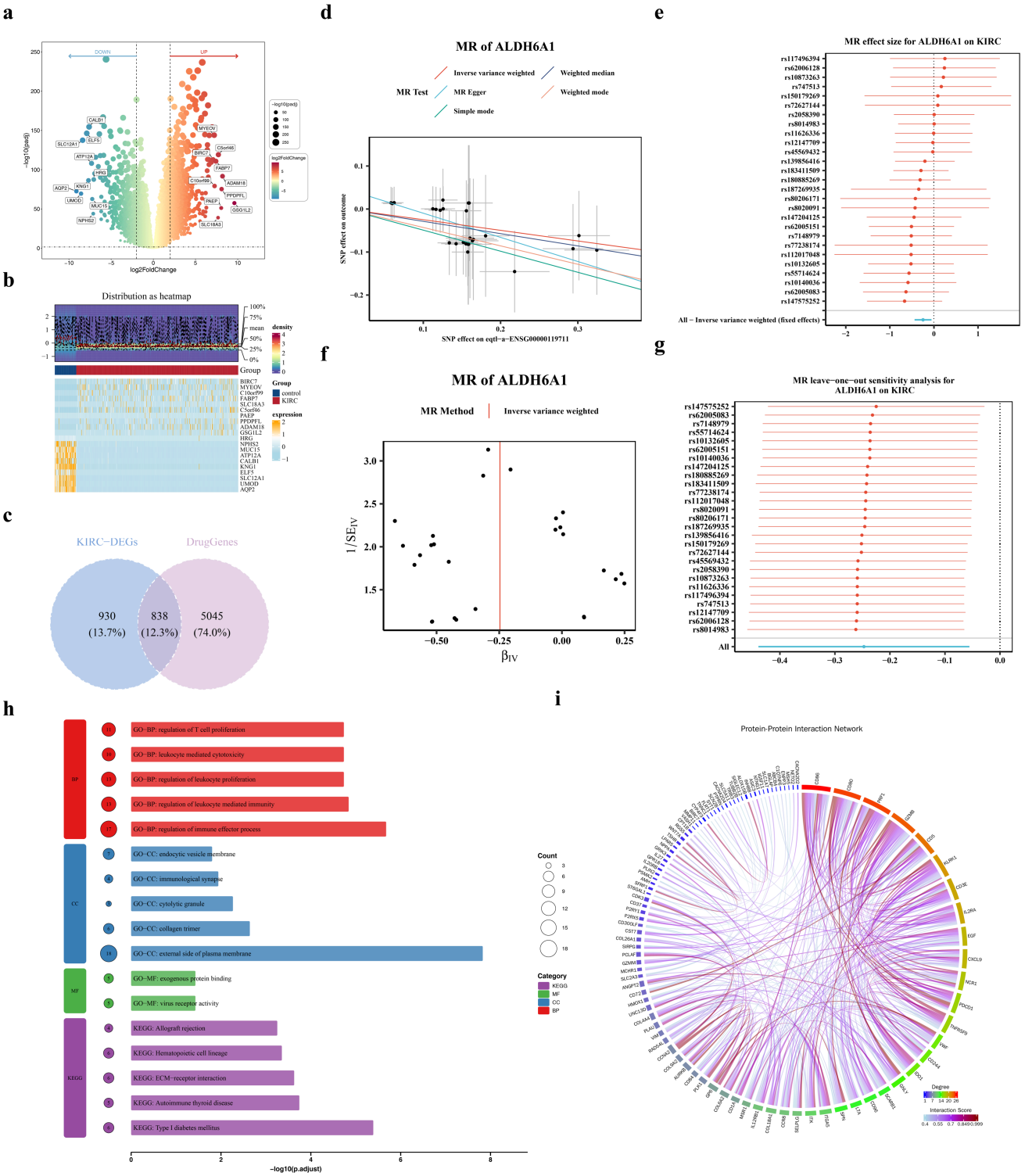


Figure 1

Identification and functional characterization of druggable genes causally linked to KIRC. (a) Volcano plot of differentially expressed genes (DEGs) in KIRC. (b) Heatmap showing expression of the top 20 DEGs. (c) Venn diagram identifying 838 candidate genes at the intersection of DEGs and the druggable genome. (d-g) Mendelian Randomization analysis validates ALDH6A1 as a protective factor: (d) Scatter plot, (e) Forest plot, (f) Funnel plot, (g) Leave-one-out sensitivity analysis. (h) Functional enrichment

analysis of the 129 candidate genes in immune-related and oncogenic pathways. (i) Protein-protein interaction network of the candidate genes.

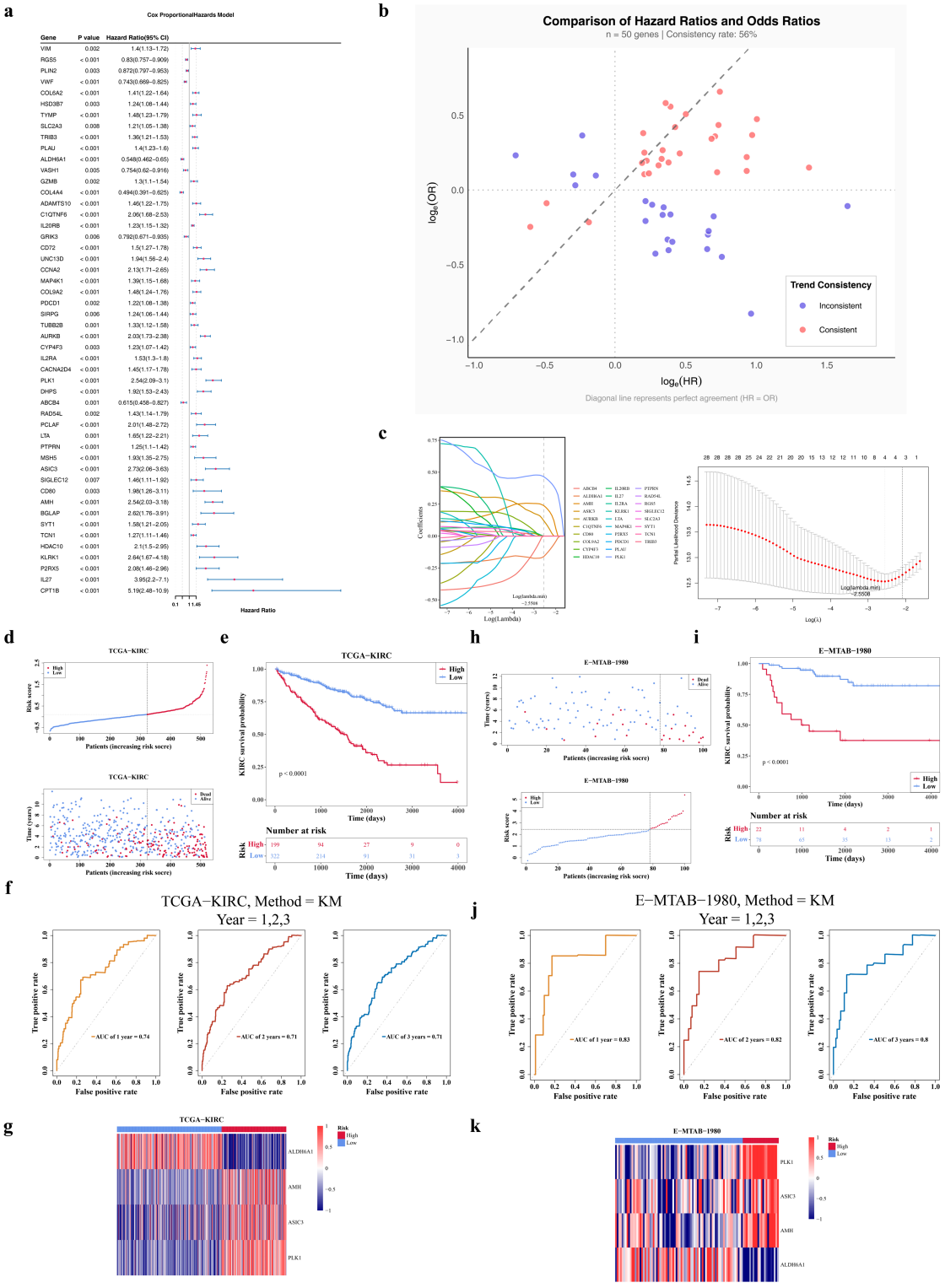
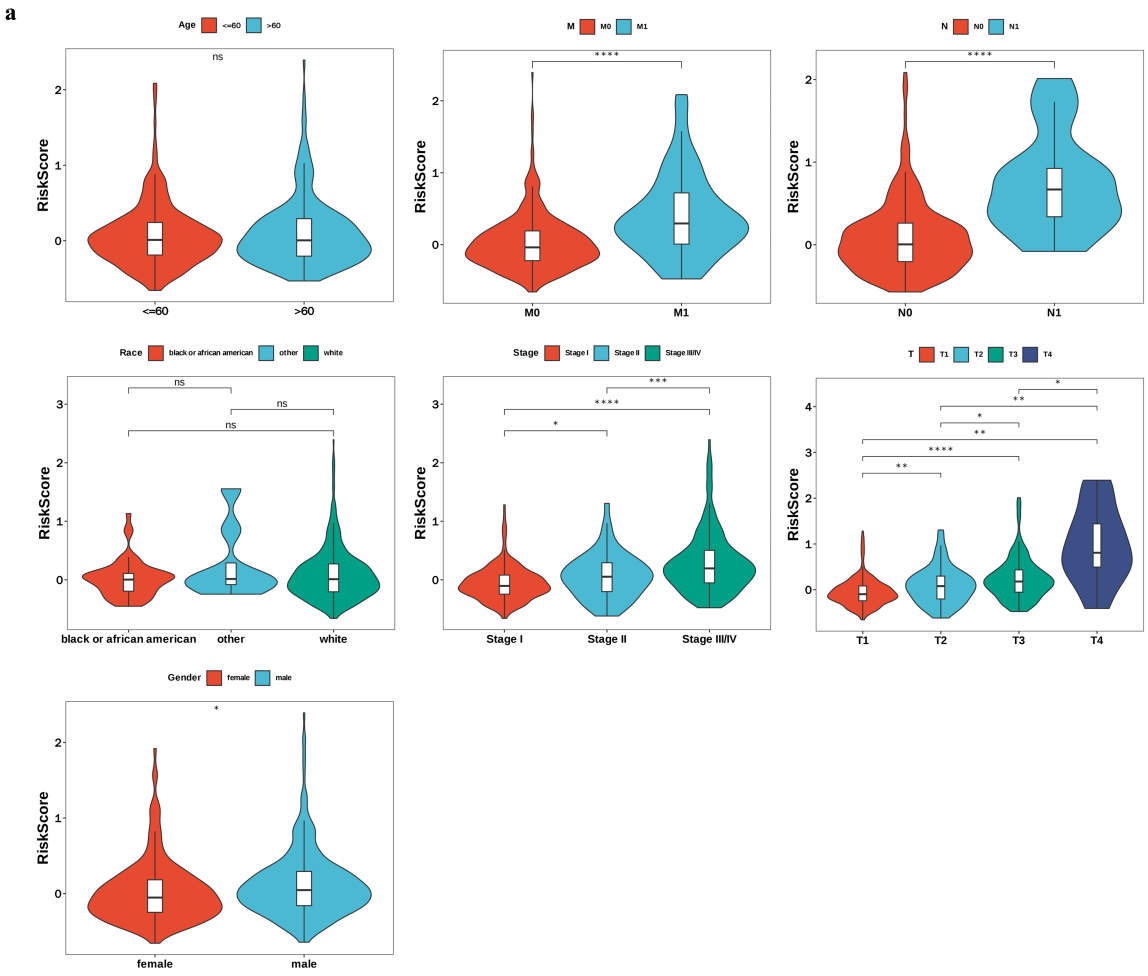


Figure 2

Construction and validation of a druggable gene-based risk model for KIRC prognosis. (a) 50 prognosis-related candidate genes identified by univariate Cox analysis. (b) Venn diagram intersecting

prognosis- and MR-associated genes, yielding 28 consistent genes. (c) LASSO regression coefficient profiles, identifying four genes (*ALDH6A1*, *AMH*, *ASIC3*, *PLK1*) for the final signature. (d) Distribution of risk scores and patient stratification into high- and low-risk groups. (e) Kaplan-Meier survival curves showing significantly worse outcomes in the high-risk group ($p < 0.0001$). (f) Time-dependent ROC curves demonstrating the model's predictive accuracy (1-/2-/3-year AUC > 0.70). (g) Expression levels of the four signature genes in high- vs. low-risk groups.(h-k) External validation of the risk model's stratification efficacy.



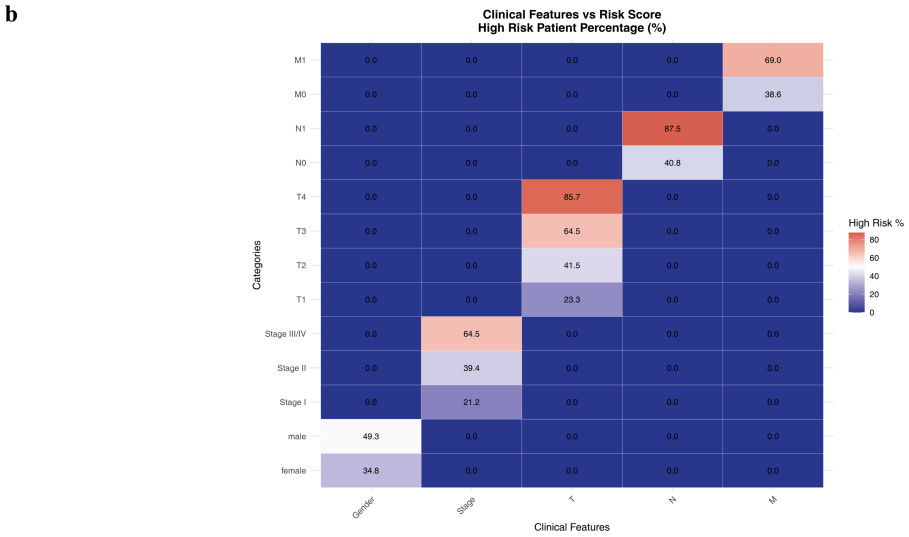


Figure 3

Association of the risk score with clinicopathological features. (a) Correlation heatmap between risk score and key clinical indicators. (b) Violin plots showing risk scores are significantly elevated in male patients and advanced-stage tumors.

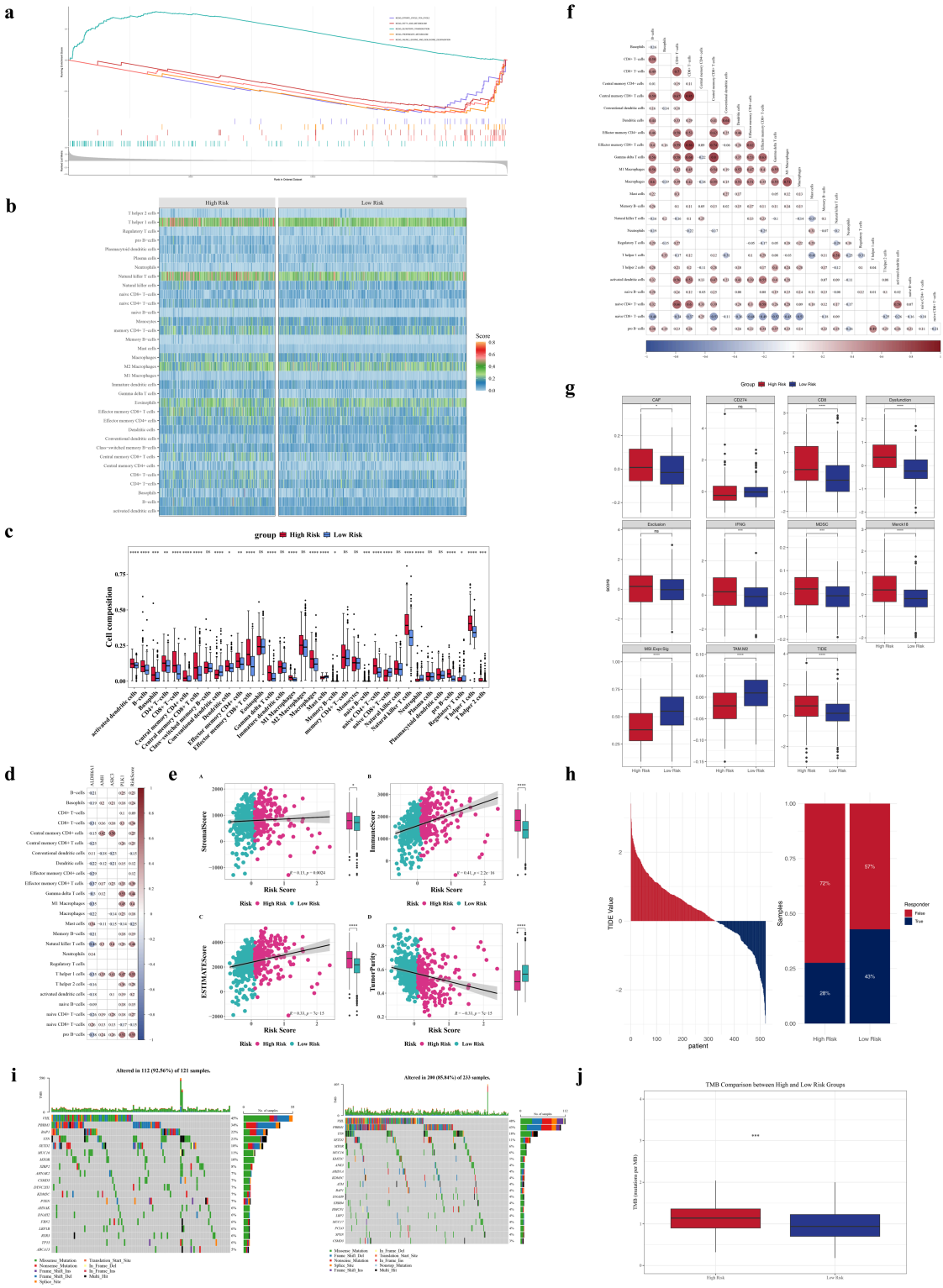


Figure 4

Immune microenvironment characterization and somatic mutation profiling stratified by the druggable gene-based risk model. (a) Pathway enrichment analysis of DEGs between risk groups. (b) Heatmap showing the infiltration patterns of 34 immune cell types. (c) Comparison of differential immune cell infiltration between high- and low-risk groups. (d) Correlation network among differentially infiltrated immune cells. (e) Correlation heatmap between prognostic genes (and risk score) and key immune cells. (f) Comparison of tumor microenvironment scores (ESTIMATE, immune, stromal) and tumor purity between risk groups. (g) Comparison of immunotherapy response-related features (e.g., TIDE, CAFs, dysfunction score) between risk groups. (h) Bar chart comparing predicted response rates to immunotherapy between risk groups. (i) Oncoplots depicting the landscape of somatic mutations in high- and low-risk groups. (j) Violin plots comparing tumor mutation burden (TMB) distribution between risk groups.

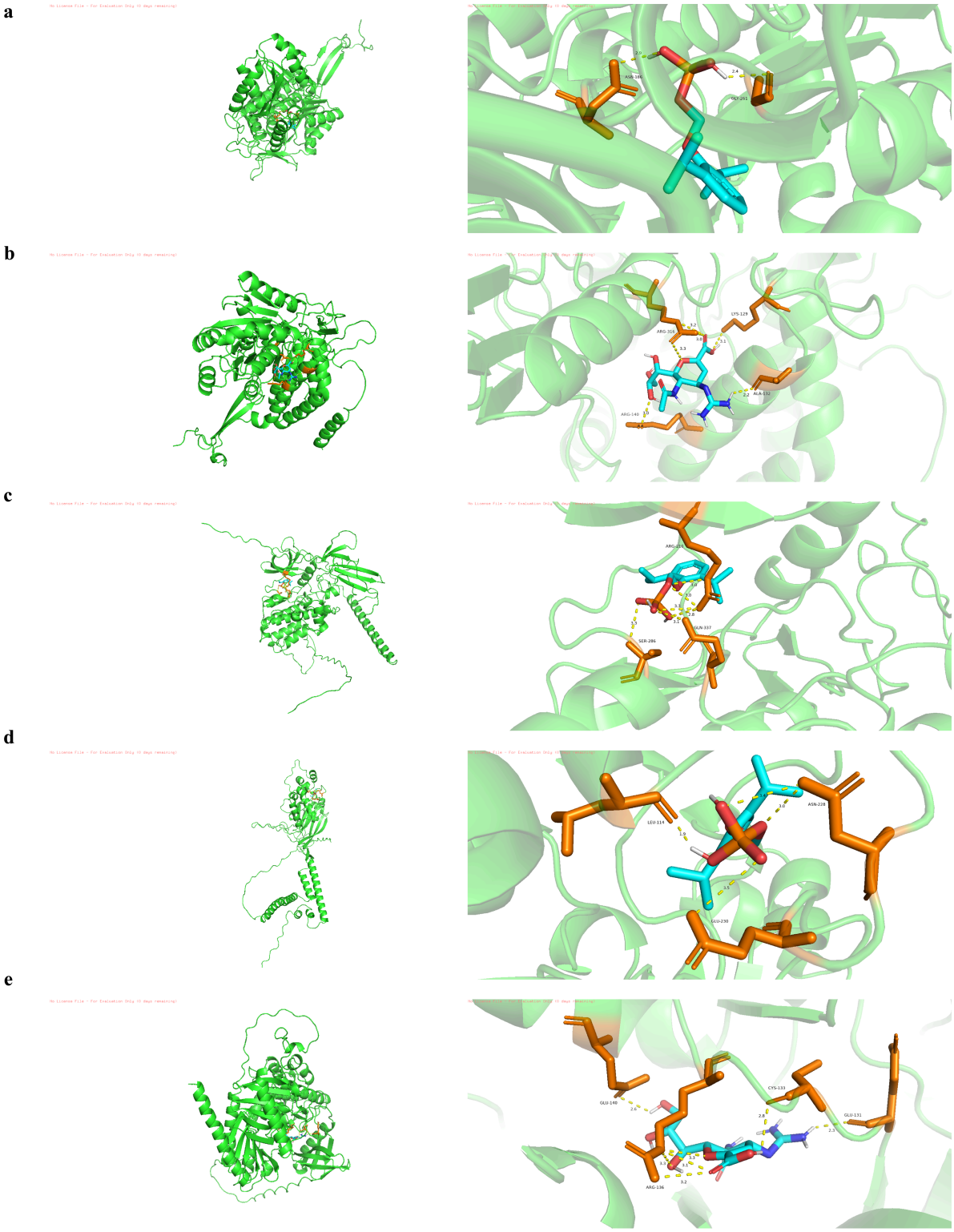


Figure 5

Prediction and validation of candidate drug interactions with the prognostic genes. (a–e) Predicted binding modes and calculated binding affinities (kcal/mol) between the four prognostic proteins (*ALDH6A1*, *AMH*, *ASIC3*, *PLK1*) and candidate drugs (fospropofol, zanamivir).



Figure 6

Molecular dynamics simulations confirm the stability of the drug-protein complexes. (a) Root-mean-square deviation (RMSD) trajectories of the complexes over 100 ns. (b) Root-mean-square fluctuation (RMSF) per residue, indicating protein flexibility. (c) Total energy of the simulated systems throughout the production run. (d) Number of hydrogen bonds formed between the drugs and proteins over time.

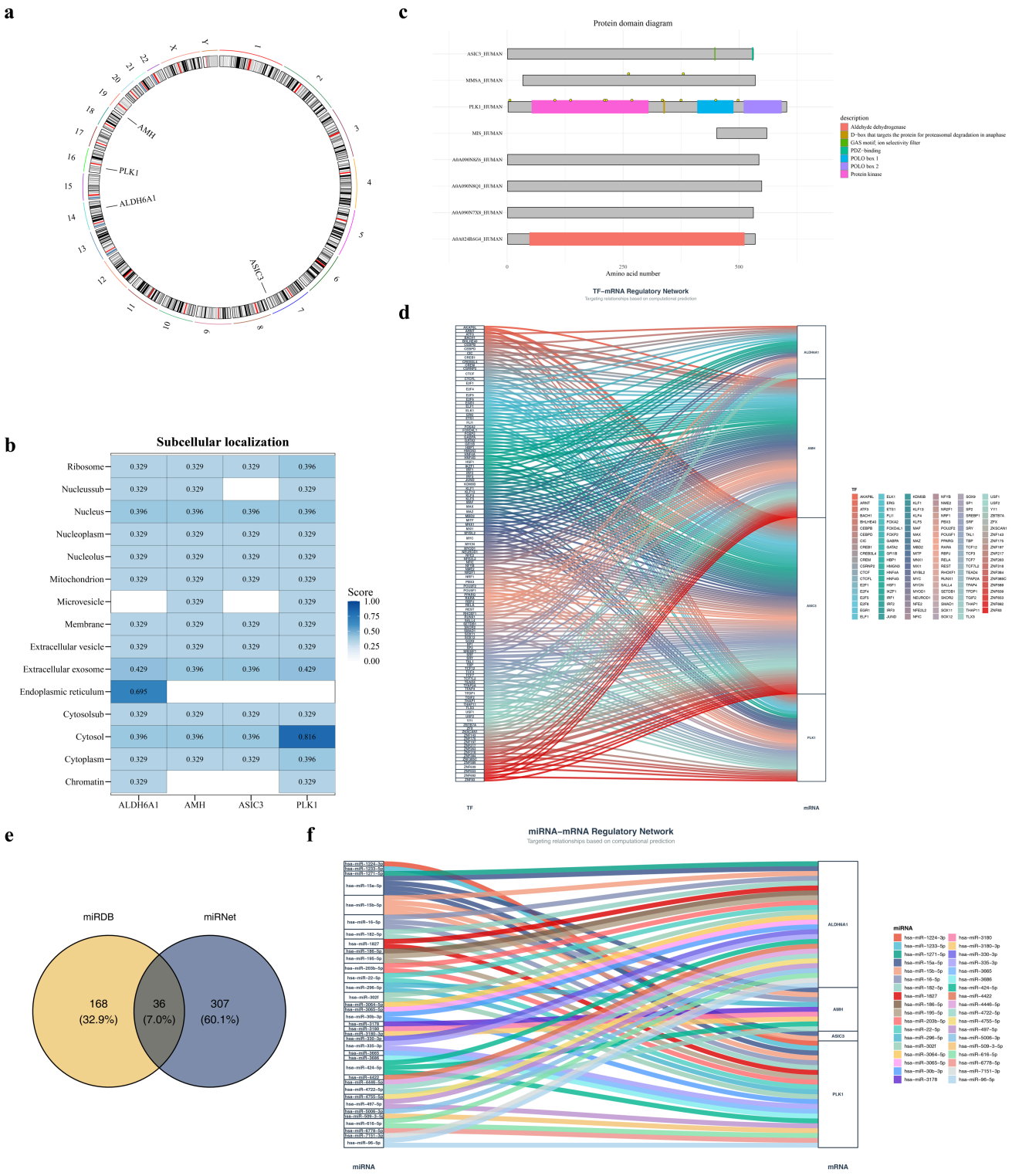


Figure 7

Molecular characterization and regulatory networks of the four prognostic druggable genes. (a) Chromosomal localization of *ASIC3*, *ALDH6A1*, *PLK1*, and *AMH*. (b) Predicted subcellular localization scores for each gene product. (c) Schematic representation of functional domains, modification sites, and key motifs within the encoded protein sequences. (d) Transcriptional regulatory network, highlighting transcription factors (e.g., CTCF, E2F4, MYC) that co-target all four genes. (e-f) miRNA-mRNA

regulatory network, identifying shared miRNAs (e.g., hsa-miR-15a/b-5p) that potentially regulate the prognostic genes.

Supplementary Files

This is a list of supplementary files associated with this preprint. Click to download.

- SupplementaryTable1.xlsx
- SupplementaryTable2.xlsx
- SupplementaryTable3.xlsx
- SupplementaryTable4.xlsx
- SupplementaryTable5.xlsx
- SupplementaryTable6.xlsx
- SupplementaryTable7.xlsx
- SupplementaryTable8.xlsx
- SupplementaryTable9.xlsx
- SupplementaryTable10.xlsx